doi:10.1016/j.jmb.2007.02.070 J. Mol. Biol. (2007) 368, 607–617

JMB

Available online at www.sciencedirect.com

ScienceDirect

ELSEVIER

Structural Basis of Aquaporin Inhibition by Mercury

David F. Savage[1]* and Robert M. Stroud[2]

[1]*Graduate Group in Biophysics University of California at San Francisco, San Francisco CA 94158, USA*

[2]*Department of Biochemistry and Biophysics, University of California at San Francisco San Francisco, CA 94158, USA*

**Corresponding author*

The aquaporin family of channels was defined based on the inhibition of water transport by mercurial compounds. Despite the important role of mercurials, little is known about the structural changes involved upon mercury binding leading to channel inhibition. To elucidate the mechanism we designed a mutant, T183C, of aquaporin Z (AqpZ) patterned after the known mercury-sensitive site of aquaporin 1 (AQP1) and determined the X-ray crystal structures of the unbound and mercury blocked states. Superposition of the two structures shows no conformational rearrangement upon mercury binding. In the blocked structure, there are two mercury sites, one bound to Cys183 and occluding the pore, and a second, also bound to the same cysteine but found buried in an interstitial cavity. To test the mechanism of blockade we designed a different mutant, L170C, to produce a more effective mercury block at the pore site. In a dose-response inhibition study, this mutant was 20 times more sensitive to mercury than wild-type AqpZ and four times more sensitive than T183C. The X-ray structure of L170C shows four mercury atoms at, or near, the pore site defined in the T183C structure and no structural change upon mercury binding. Thus, we elucidate a steric inhibition mechanism for this important class of channels by mercury.

Keywords: aquaporin; integral membrane protein; X-ray crystallography; membrane protein structure

Introduction

Aquaporins (AQPs) are integral membrane channel proteins that mediate the bi-directional flux of water and selected small amphipathic molecules across cellular membranes.[1] In the field of channel biology, selective inhibitors including naturally occurring toxins and organic molecules have played key roles in defining function,[2] but AQPs have no such specialized inhibitors. Mercurial compounds were found to reduce water transport in the red blood cell membrane to that of a bilayer and so defined the presence of a cellular water channel.[3] This selective inhibition subsequently allowed for aquaporin isolation,[4] cloning,[5,6] membrane transport characterization,[7] and mercury sensitivity mutational analysis.[8,9] The precise mechanism of AQP inhibition by mercury is still undetermined.

The AQP fold is a right-handed bundle of six transmembrane (TM) helices and two half-spanning helices (named M1–M8) with the pore running through the center of the helical bundle. There is a quasi 2-fold symmetric relationship between the N-terminal portion of the polypeptide chain (M1–M4) and the C-terminal portion (M5–M8) from early gene duplication. In the membrane, AQPs occur as homotetramers of four monomer channels related by a 4-fold symmetry axis (Figure 1(a)). The AQP family is divided into two subfamilies, the water selective channels and those with a more promiscuous selectivity for both water and other small amphipathic molecules such as glycerol (aquaglyceroporins).[13] A comparison of GlpF, AQP1, and the other recently determined structures, shows that the AQP fold is conserved.[14–17] AQPs are identified by two asparagine-proline-alanine (NPA) sequence motifs located at the ends of the two quasi 2-fold related half-spanning helices M3 and M7 (Figure 1(b)). The selectivity filter, a constricted region formed by four residues near the periplasmic/extracellular entrance, provides distinguishing

Abbreviations used: AQP1, aquaporin 1; AqpZ, aquaporin Z; TM, transmembrane; GlpF, glycerol facilitator; WT, wild-type; IC_{50}, half maximal inhibitory concentration; RMSD, root mean square deviation; BME, 2-mercaptoethanol; AD, anomalous diffraction; RT, room temperature.

E-mail address of the corresponding author: savage@msg.ucsf.edu

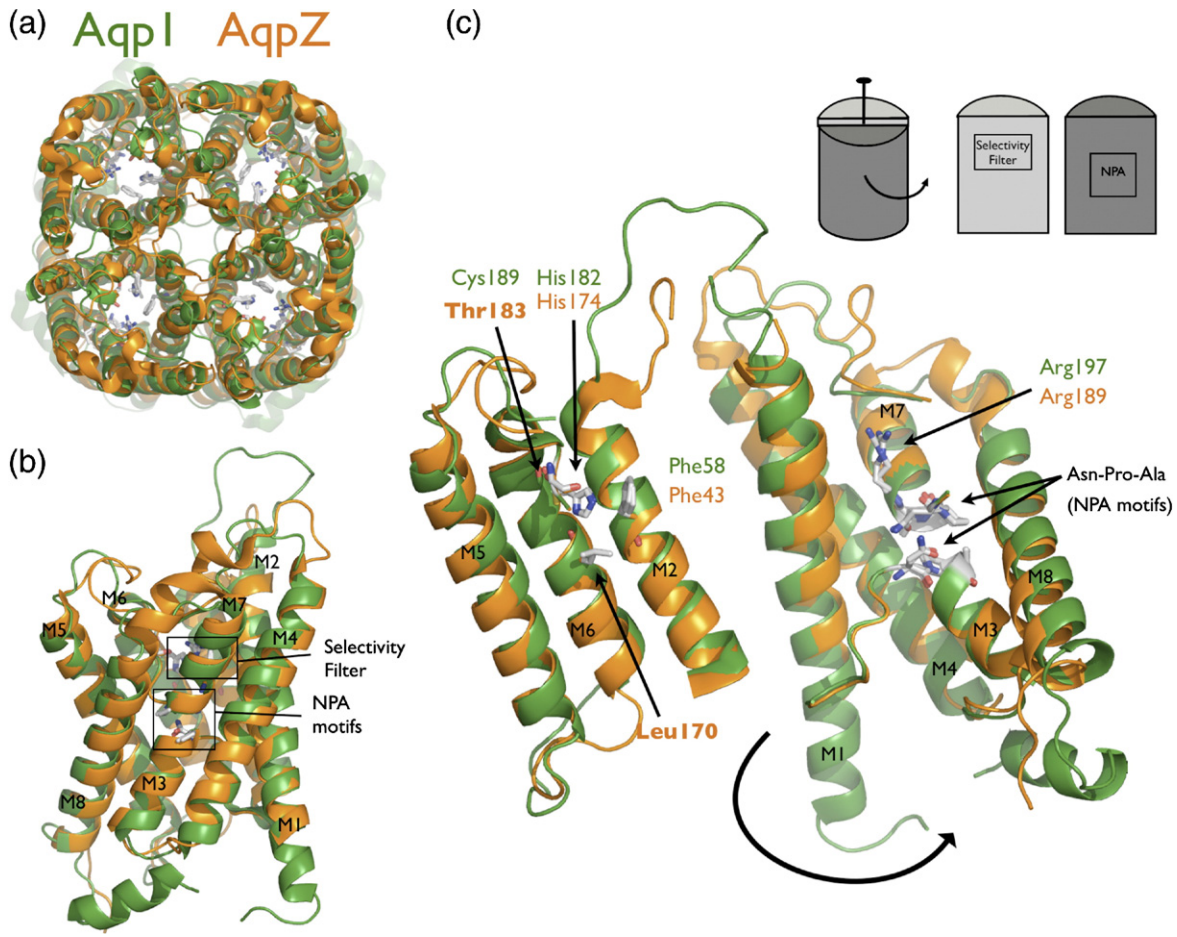

Figure 1. AqpZ is the bacterial homolog of AQP1. (a) Cartoon representation of the AqpZ (orange) and AQP1 (green) tetramers. Note the presence of the four monomer channels and the hypothetical channel down the tetramer axis. (b) Cartoon representation of the AqpZ and AQP1 monomers. Helices are labeled M1 through M8, and the selectivity filter and NPA motifs are designated with boxes. (c) Monomer opened up showing conservation of the water-selective motif. In this cartoon representation, the monomer is peeled open as shown in the inset schematic. The conserved selectivity filter and NPA motif are shown in sticks. Thr183 and Leu170 in AqpZ are the positions of cysteine mutants in this study. All molecular structure Figures were made in Pymol (Delano Scientific).

features that identify the subfamilies (Figure 1(b) and (c)). In water selective AQPs this region is smaller and more polar and contains a conserved histidine, while in aquaglyceroporins it is larger and more hydrophobic with two conserved aromatic residues.[13] Thus, the AQP architecture is conserved and it is the pore side-chains that modulate specific functional differences (Figure 1(c)).

Mercurials can bind non-selectively to accessible cysteine residues, but in AQPs, due to a decrease in solvent accessibility from the membrane bilayer, mercury typically binds selectively to residues associated with the pore. In the mutational analysis of AQP1, removal of endogenous cysteine residues identified Cys189 as the one responsible for mercury sensitivity and predicted its pore location. Confirmation of Cys189 as a pore residue came from the first atomic resolution AQP structure, that of the *Escherichia coli* glycerol channel (GlpF),[10] and the later AQP1 structure[11,12] showed precisely how the cysteine, not present in the GlpF sequence, was oriented. The structure of AQP1 was determined with protein obtained from natural sources so is not conveniently amenable to mutation and mercury was not used in the structural analysis. To understand the mechanism of mercury inhibition in AQPs we focused our efforts on the bacterial homolog of AQP1, AqpZ.[18] AqpZ contains the water-selective sequence motif of AQP1 at the selectivity filter, has functionally been described as a water channel,[19] is not mercury sensitive, can be over-expressed and mutated, and its X-ray structure has previously been determined in our laboratory. AqpZ is thus a useful model system for probing the relationship between structure and function (Figure 1).[14,20]

Results

Structure of mutant T183C complexed with mercury

AqpZ and AQP1 are both functionally characterized as water-selective channels and have an identical selectivity filter except that AqpZ lacks

the well-described mercury-sensitive cysteine of AQP1 (Thr183 in AqpZ, Cys189 in AQP1). Based on this similarity, we postulated that a mutant of AqpZ lacking all endogenous cysteine residues but including the known mercury-sensitive site of AQP1, would serve as a model for AQP1 (Figure 1(c)). The two endogenous cysteine residues of AqpZ were replaced with serine by mutagenesis, and the AQP1 mercury-sensitive site was introduced *via* mutation Thr183Cys (protein hereby denoted T183C). This mutant, T183C, was expressed, purified, and crystallized in the presence or absence of $HgCl_2$ to determine the structural implications of mercury binding. The crystals diffracted to atomic resolution, and the two structures were solved by molecular replacement using the previously published structure of WT AqpZ (Protein Data Bank (PDB) code 1RC2).[14] The final resolution cutoffs were 2.30 Å and 2.20 Å, and the R_{free} statistics for the refined structures were 23.8% and 24.2% for the apo and mercury-bound forms, respectively (Table 1). The overall structures of both the apo and complexed forms display the canonical AQP fold (Figure 2(a) and (b)).[10] Superposition of the structures shows that there is no significant conformational change between the two forms, and the root mean square deviation (RMSD) of the main chain α-carbon atoms is 0.27 Å.

A calculation of the channel surface (Figure 2(c)) using van der Waals radii with the program HOLE2[21] reveals a 20 Å long pore resembling the wild-type (WT) structure. The most striking feature of the complex structure is the two large electron density peaks of the mercury atoms and their unexpected location; one is located directly in the pore and one is interstitially bound in a cavity just outside the pore (Figure 2(c)). T183C-Hg1 (nomenclature is mutant followed by mercury atom number), the mercury in the pore, is located roughly halfway between the NPA region and the narrow selectivity filter. It makes favorable electrostatic contacts with the main chain carbonyl of S184 (3.3 Å) and the imidazole ring of His174 (3.7 Å). Somewhat surprisingly, T183C-Hg1 is approximately 5.6 Å away from Cys183 and is 3.9 Å to the closest water. T183C-Hg2, the mercury outside of the pore, is bound to Cys183 (distance of 4.0 Å) and resides in a hydrophilic pocket formed by conserved Glu138 and Ser177 where it makes favorable electrostatic interactions of 2.6 Å and 3.1 Å, respectively.

The thiol–mercury bond distances are considerably longer than the ideal length of 2.5 Å and noise in difference maps suggests that both mercury atoms are disordered and at partial occupancy. We therefore carried out joint occupancy and anisotropic *B*-factor refinement in SHELX.[22] In this calculation, T183C-Hg1 and T183C-Hg2 refine to occupancies of 0.24 and 0.32, respectively, suggesting a higher affinity or less disorder at the interstitial site. The anisotropic displacement parameters for T183C-Hg1 suggest disorder parallel to the channel axis, while T183C-Hg2 is disordered between residues Glu138 and Cys183. This disorder can also be observed in the $2F_o–F_c$ electron density (Figure 2(c)).

Based on these results, we hypothesized that the mercury site in the pore produces a steric block of the channel. To test this hypothesis we designed an optimized mercury-binding site in the pore, to provide a "switch" as a probe of conductance in AqpZ. This new mutation, Leu170Cys in the cysteine-less background, was intended to bind mercury only at the site within the pore. We next biophysically characterized WT, T183C, and L170C to determine their relative mercury sensitivities.

Table 1. Crystallographic data and refinement statistics

	T183C	T183C-Mercury	L170C	L170C-Mercury
Data collection				
Space group	*P*4	*I*4	*P*4	*I*4
Unit cell				
a (Å)	92.4	91.1	91.3	91.2
c (Å)	78.2	77.9	77.5	77.1
Resolution range (Å)[a]	50–2.30 (2.30–2.36)	50–2.20 (2.20–2.26)	50–2.55 (2.55–2.62)	50–1.90 (19.0–1.95)
Unique reflections	28,897	16,199	15,206	23,096
Completeness[a]	98.3 (93.8)	99.8 (100.0)	74.1 (65.5)	92.8 (66.4)
R_{sym}[b] (%)[a]	7.3 (59.5)	8.8 (59.5)	7.5 (46.2)	6.4 (33.4)
$I/\sigma(I)$[a]	15.3 (1.1)	15.5 (1.9)	10.3 (1.2)	15.4 (1.7)
Refinement statistics				
R_{work}/R_{free} (%)	19.7/23.8	19.3/24.2	23.6/28.0	16.6/19.5
RMSD bonds (Å)[c]	0.016	0.015	0.012	0.014
RMSD angles (°)[c]	1.65	1.64	1.45	1.61
Number of protein atoms	3356	1671	3368	1696
Number of solvent atoms	109	68	43	139
Number of Hg atoms	0	3	0	4
Average *B*-factor (Å^2)	37.7	36.4	24.9	23.2
PDB code	209D	209E	209F	209G

[a] Values in parenthesis refer to the highest-resolution shell.
[b] $\sum |I—\langle I\rangle| / \sum I$, where *I* equals observed intensity and $\langle I\rangle$ equals average intensity for symmetry-related reflections.
[c] Root-mean-square deviation of bond lengths and angles from ideal values.

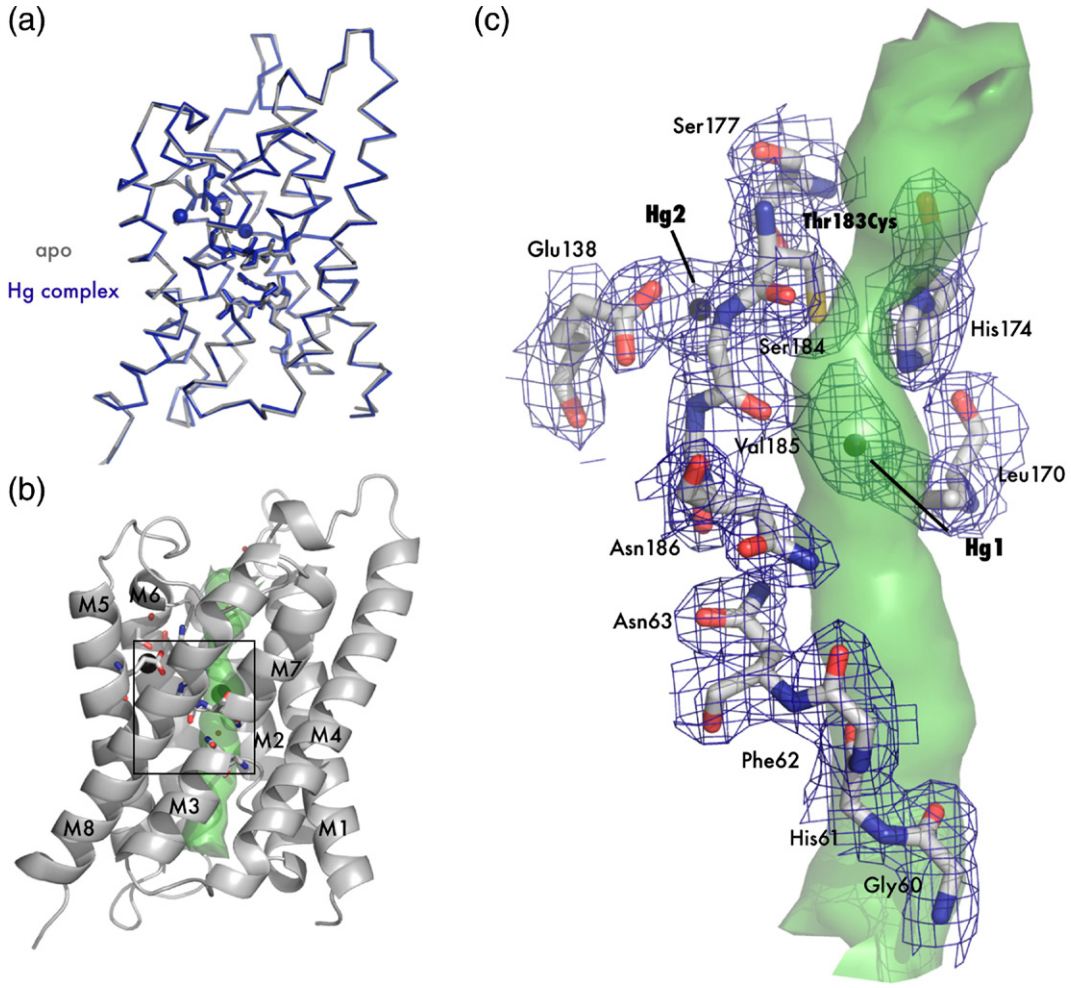

Figure 2. Crystal structure of apo T183C and mercury bound T183C mutants. (a) Main chain overlay of the apo (gray) and Hg-complex (blue) with an RMSD (C^{α}) of 0.27 Å. Bound Hg^{2+} atoms are displayed as spheres with a van der Waals radius of 1.10 Å. (b) Cartoon representation of T183C. Transmembrane helices are labeled M1–M8 and the interior surface of the channel is drawn as a green surface. The black square denotes the area of interest depicted in (c). (c) Structure of the blocked channel. Amino acids involved with water binding in AQPs are shown as sticks and with $2F_o–F_c$ electron density mapped contoured at 1.2σ drawn in blue. Mercury atoms are shown as spheres. In this orientation it can be seen that T183C-Hg1 sterically blocks the pore (green surface).

Kinetics of water flux and mercury inhibition

Flux through the AQP channel was assayed in osmotically driven liposome permeability experiments.[19] AqpZ is a water-selective channel with high rates of conduction and we first sought to determine the activity of WT, T183C, and L170C. Purified proteins were reconstituted into liposomes and kinetics assayed in a stopped-flow device by mixing proteoliposomes with a hyperosmolar reconstitution buffer to drive water efflux. The resulting proteoliposome shrinkage was measured by light scattering and the curve fit to an exponential equation with a single rate constant. Raw light scattering data are provided in Figure 3(a), along with the fitted curves. We measured the rates of WT, T183C, and L170C to be 73.9(±0.4) (standard deviation) s^{-1}, 57.3(±0.5) s^{-1} and 39.0(±0.4) s^{-1}, respectively, indicating that all proteins are functional water channels. Thus, WT has the fastest rate of conduction, T183C is slightly slower, and L170C much slower. Control liposomes without protein had rates of 4.6(±0.1) s^{-1}.

In order to ascertain the role of $HgCl_2$ as an inhibitor we determined the half maximal inhibitory concentration (IC_{50}) using a dose-response relationship. In this experiment proteoliposomes were incubated with various concentrations of $HgCl_2$ and then assayed for water conduction as described above. The results (Figure 3(b)) demonstrate that WT is the most sensitive to inhibition by mercury. The mutants, as expected, are inhibited at progressively lower concentrations with IC_{50}s of 345 μM, 84 μM, and 18 μM for WT, T183C and L170C, respectively,[19] and thus, L170C is the most sensitive to mercury. $HgCl_2$ did not affect control liposomes and mercury inhibition was reversible with the addition of 5 mM 2-mercaptoethanol (BME) following mercury incubation (data not shown).

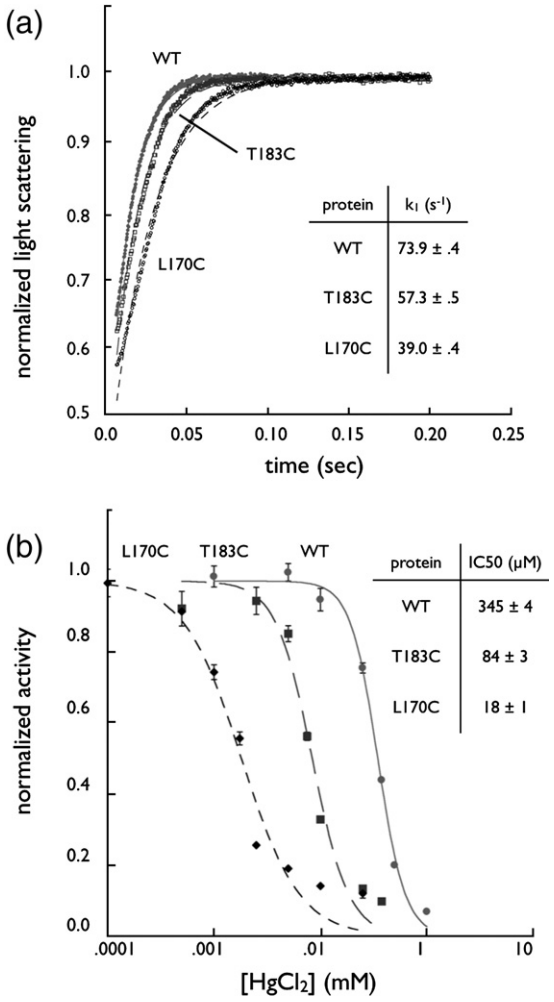

Figure 3. Kinetic studies of aquaporin Z. (a) Water conduction of WT, T170C, and T183C. Proteins were reconstituted in liposomes, challenged with a higher osmotic gradient in a stopped-flow device, and liposome shrinkage measured by light scattering at 440 nm. Plots were fit to a single exponential and the resulting rates are shown in the inset table ($n=5$). (b) Dose-response curve of proteoliposomes incubated with $HgCl_2$. After incubation with $HgCl_2$ proteoliposomes were assayed as in (a) and the rates (normalized to maximum rate for each mutant, $n=5$) were fit to a sigmoid dose-response curve in Kaleidagraph (Synergy Software). IC_{50} values are shown in the inset table.

Structure of mutant L170C blocked by mercury

Since L170C has a heightened sensitivity to mercury we determined the X-ray structure of the apo and complex forms. L170C was over-expressed, purified, and crystallized with and without mercury using $HgCl_2$ as an additive. Diffraction data were collected to 2.55 Å and 1.90 Å for the apo and complex proteins, respectively, and the structures were solved by molecular replacement. As described in Materials and Methods, the model was built and refined iteratively to an R_{free} of 28.0% and 19.5% for the apo and complex forms, respectively (Table 1). Like T183C, L170C displays the same AQP canonical fold, and also like T183C, shows very little structural difference between the apo and complex form. The superposition (RMSD 0.27 Å) is shown in Figure 4(a).

As we predicted, introduction of a cysteine residue at position 170 increases the affinity at the T183C-Hg1 site, and we were able to locate four mercury atoms (named L170C-Hg1, L170C-Hg2, L170C-Hg3, and L170C-Hg4) near the NPA region between Cys170 and His174. These atoms are clustered together, as indicated in the channel pathway of Figure 4(b) and (c). L170C-Hg2, L170C-Hg3, and L170C-Hg4 lie directly in the pore, while L170C-Hg1 is at the edge (Figure 4(c)). The occupancies of L170C-Hg1, L170C-Hg2, L170C-Hg3, and L170C-Hg4 were refined to 0.40, 0.23, 0.20, and 0.18, respectively. L170C-Hg2 is covalently bound to Cys170 at the distance expected for a sulfur–mercury bond length (2.6 Å). L170C-Hg2 is also at the proper Hg dinuclear complex distance from L170C-Hg1 (2.5 Å), L170C-Hg3 (2.3 Å), and L170C-Hg4 (2.4 Å) and there is continuous electron density between all mercury atoms at 1.5 σ in a $2F_o–F_c$ map. L170C-Hg2 may therefore mediate the binding of a second mercury in the pore at any of the three other positions. L170C-Hg3 lies directly in the pore at the same site as T183C-Hg1 (magenta double cross in Figure 4(c)) and may interact with the imidazole ring of H174 (3.8 Å) in a similar manner.

Discussion

Aquaporins and mercury inhibition

Even after the knowledge of the extreme toxicity of mercury and its various compounds, it continued to find use in disinfectants, cosmetics, and a suite of so-called medicines.[23] Mercurials attack the reactive thiol moiety of cysteine found in nearly all proteins and are known to have a host of side effects including polyuria induced by AQP2 inhibition in the apical membrane of the kidney collection tubule.[24] Due to its affinity for thiols, mercury has been useful in chemical probes of protein-mediated biological processes, as it was in defining the water channels as proteins. Mercury as a pore blocker has been instrumental in characterizing the AQP channel and revealing the role of AQPs in membrane transport for numerous tissues.[6,7]

Steric inhibition by mercury

We located two mercury atoms in the T183C-mercury complex X-ray structure. These atoms, T183C-Hg1 and T183C-Hg2, are located in the pore and at an interstitial site, respectively. Given that T183C is four times more sensitive to mercury than WT, we sought to establish the relevance of each site to this important functional result and therefore determine whether the mechanism is steric or rooted in conformational rearrangement.

The most obvious explanation for inhibition is that T183C-Hg1, due to its location, directly blocks the

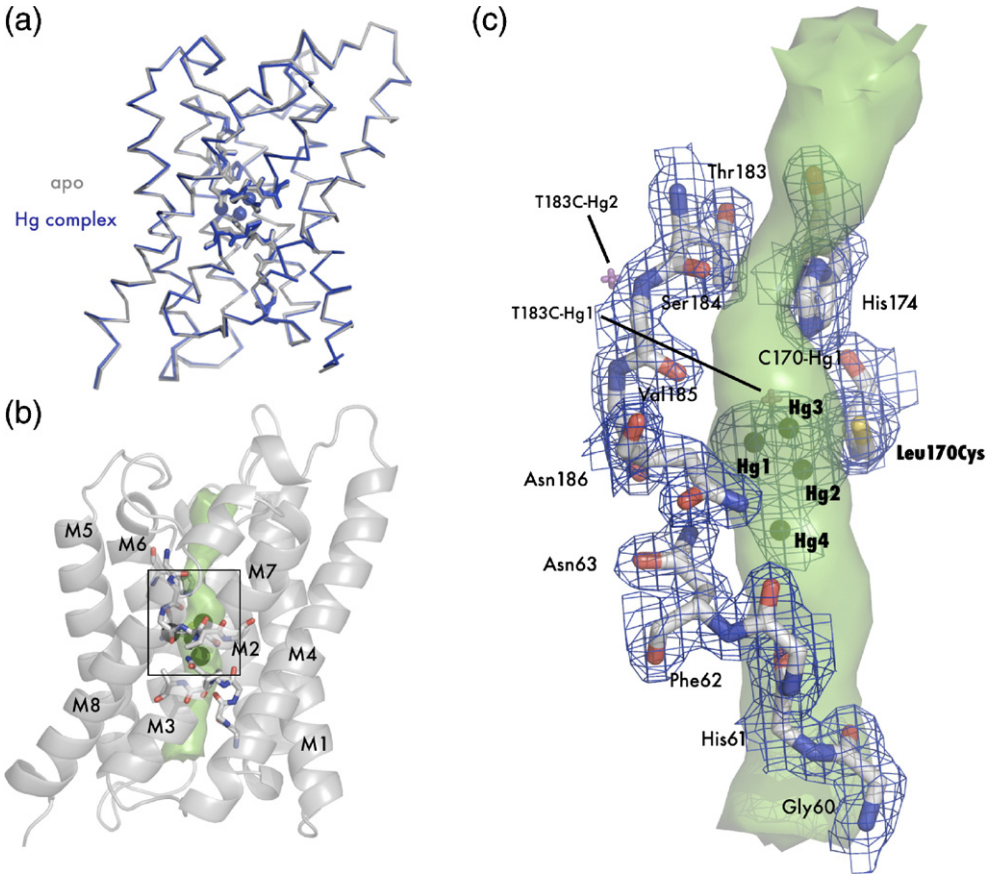

Figure 4. Crystal structure of apo L170C and mercury bound L170C. (a) Main chain overlay of the apo (gray) and Hg-complex (blue) with an RMSD of 0.27 Å. Bound mercury atoms are displayed as spheres with a van der Waals radius of 1.10 Å. (b) Cartoon representation of L170C. Transmembrane helices are labeled M1–M8 and the interior surface of the channel is drawn as a green surface. The black square denotes the area of interest depicted in (c). (c) Structure of the blocked channel. Amino acids classically involved with water binding in AQPs are shown as sticks and with $2F_o$–F_c electron density mapped contoured at 1.2 σ drawn in blue. Mercury atoms are shown as spheres. Superpositions of mercury atoms from the T183C structure are shown as magenta crosses. In this orientation it can be seen that all three mercury atoms sterically block the pore (green surface).

pore and inhibits through a steric mechanism. This is further supported by the fact that there is little structural change between the apo and mercury-complexed forms (Figure 2(a)). Divalent mercury has a small ionic radius of 1.10 Å, which would explain the lack of structural perturbation and its ability to bind deep within the protein (T183C-Hg2). But, while steric blockage is both supported by the data and simple, can we rule out conformational change?

Occupancy refinement revealed that both T183C-Hg1 and T183C-Hg2 are present at significantly less than unity (0.24 and 0.32, respectively). Since the mercury sites are of low occupancy, they may occur (i) alternately in different channels, i.e. they may be exclusive of one another, or (ii) they may both be bound, either cooperatively or uncooperatively, and have a lower occupancy for reasons outlined below. In either case, any changes in the protein around a partially occupied site would also be of low (~0.3) occupancy, and so be difficult to refine as multiple conformers. This could be particularly important for T183C-Hg2, bound to the highly conserved Glu138. Rearrangement of Glu138 could perturb the essential water-coordinating carbonyl groups and potentially disrupt water flux. However, inspection of F_o–F_c difference maps reveals an increased noise level (Figure 6(a) and (b)), but no obvious alternate conformer. Also the potentially cleaner F_o(apo)–F_o(Hg) maps between observations *per se* were not possible due to the degree of lack of isomorphism (Table 1). Thus, distinguishing between a steric mechanism and one involving a conformational change of the protein is difficult.

Favoring the more simple steric mechanism, we set out to show blockage occurs at the T183C-Hg1 site through creation of a new cysteine mutant. To differentiate between the steric and conformational mechanism, such a mutant should bind mercury only at the pore site. Furthermore, the lower occupancy of T183C-Hg1 and longer thiol–mercury distances (5.6 Å *versus* 4.0 Å) relative to T183C-Hg2 suggest the T183C-Hg1 interaction with Cys183 is not ideal. We can thus hypothesize that a structurally optimized mutant would also be more sensitive to mercury. In this region, the pore is formed

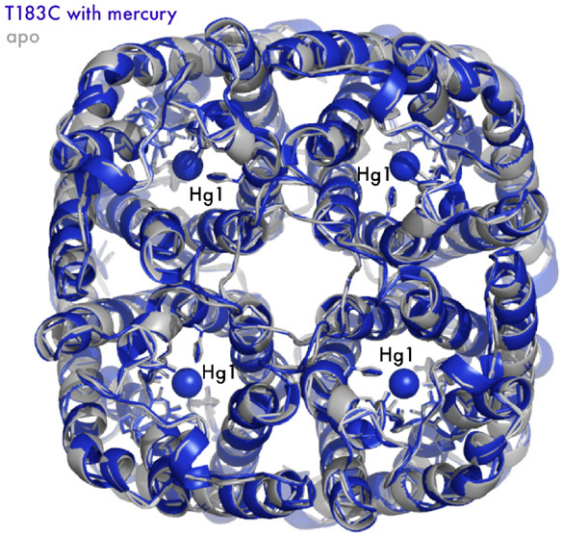

Figure 5. Mercury blocks the monomer channel. While AQPs are tetramers in the membrane, the monomer is the functional unit. By imposing crystal symmetry on both the apo (grey) and complex structures (blue), T183C is drawn as a tetramer in cartoon representation. Mercury-Hg1, with its proper van der Waals radius, is drawn as a sphere blocking the channel. Note there is almost no structural change to the tetrameric axis.

mostly by main chain water-coordinating carbonyl groups and side-chains from selectivity filter residues. Among the few side-chains that project into the pore near T183C-Hg1, Leu170 is positioned closely to the site (Figure 4(c)). Thus, mutant L170C should be functionally sensitive to mercury, only bind mercury at the pore site, and therefore support a steric blockage model.

In inhibition assay we determined that L170C, with a cysteine at the proposed steric blockage site, is actually the most sensitive to mercury with respect to WT and T183C. Furthermore, this increase in sensitivity is also echoed in the structure. As with T183C, there is little evidence of conformational change upon mercury binding. Instead, there is complete occlusion of the pore and importantly, there are no interstitially bound mercury atoms to disturb the water-coordinating carbonyl groups. There are four mercury atom positions in the pore clustered around the introduced cysteine that refine to occupancies of 0.40, 0.23, 0.20 and 0.18 for L170C-Hg1, L170C-Hg2, L170C-Hg3, and L170C-Hg4, respectively. It is therefore possible that these sites actually represent one mercury atom that is blocking the pore and is statistically disordered throughout the crystal lattice. Or, because of the low occupancy values, these sites may reflect mercury conformations that exist alternately in different blocked channels. Based on bond lengths, an attractive model is that L170C-Hg2 would be directly bound to Cys170 and then form a dinuclear mercury complex with one of three other mercury atoms. In either case, we conclude that although there may be multiple conformations of a blocked channel in L170C, the mechanism is a steric one. Finally, because the mercury atom sites in the L170C structure are at the same position as T183C-Hg1, T183C (and by analogy AQP1) may also be blocked in a steric manner.

Water permeability of AqpZ reconstituted into liposomes

Using a proteoliposome-based assay we measured the water conduction rates and determined that both mutants were active at lower conductances than for WT. While this decreased permeability may result from perturbation of the protein native state due to mutation, the decrease also appears to correlate with the introduction of a more polar cysteine side-chain into the hydrophobic pore. T183C shows a moderate decrease in rate and the cysteine rotamer points away from the pore, while L170C shows a much larger decrease and the side-chain is in the pore (Figures 2(c) and 4(c)). AQPs most likely achieve high conduction rates by partially stabilizing the substrate, similar to an idea suggested for ion channels.[27] In this case water is stabilized as a line of molecules against eight carbonyl groups, the guanidium group of Arg189, and $N^{\delta 2}$ moieties from the two conserved asparagine residues of the NPA motifs, in an otherwise hydrophobic channel. Introduction of a polar pore residue therefore increases channel water affinity and decreases flux.

Mercury and WT AqpZ

We unexpectedly discovered that WT AqpZ is also inhibited by $HgCl_2$. The WT protein contains two (Cys9 and Cys20) endogenous cysteine residues, which can presumably bind mercury, but attempts at co-crystallizing WT with mercury to justify this were unsuccessful. Problems with co-crystallization suggest non-specific binding, so the pore itself may have some low affinity for mercury due to the presence of histidine and other polar side-chains. We measured the IC_{50} of a mutant in which both endogenous cysteine residues were mutated to serine to be roughly 1 mM (data not shown). In light of this result it may be inappropriate to classify AQPs as either distinctively mercury-sensitive or insensitive. The ionic radius of Hg^{2+} is even smaller than water (1.10 Å) and so regardless of the presence of a pore cysteine, it may become partially stabilized by the partial negative charge on the carbonyl oxygen atoms and the imidazole ring of His174. Therefore, at higher (i.e. millimolar) mercury concentrations all AQPs may be inhibited. This also suggests that there may be other charged inhibitors, possibly by the mechanism outlined above.[28,29]

Mercury and the tetrameric axis

A steric mechanism with no significant structural change also validates the use of mercury to distinguish between conduction through the tetramer axis and the monomer pore. As described above,

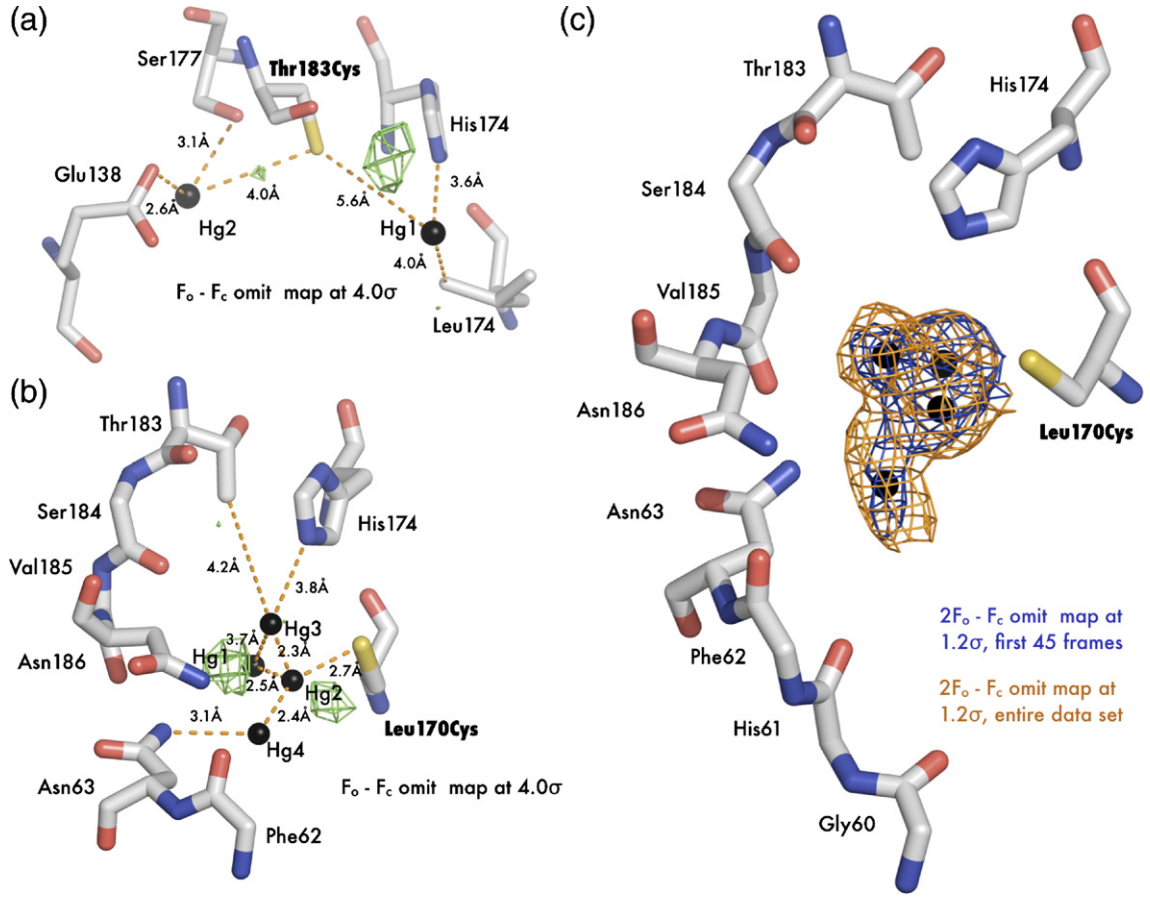

Figure 6. Mercury disorder in electron density maps. (a) F_o–F_c electron density map (green) of mercury bound T183C structure contoured at 4 σ. (b) F_o–F_c electron density map (green) of mercury bound L170C structure contoured at 4 σ. (c) $2F_o$–F_c omit electron density map solved with the first 45 frames of data (blue) and the entire dataset (orange). Both maps are contoured at 1.2 σ around the three mercury atoms.

the arrangement of the helical bundle monomer creates a 4-fold symmetric channel running parallel to the monomer channel (Figure 5). This 4-fold axis is hydrophobic, of larger dimensions than the monomer channel, and previous X-ray structures indicated the presence of some as yet undetermined molecules. Both experimental and computational studies have investigated possible substrates, including water, ions,[25] and CO_2.[26] The mercury-bound structure of T183C, along with a simple steric blockage at the proposed site, suggests that conduction studies using mercury are solely inhibiting the monomer channel.

Mercury dynamics in the pore

Mercury, due to its 80 electrons and aggressive thiol attacking nature, is one of the most common heavy atom derivatives for *de novo* phasing of X-ray crystal structures *via* isomorphous replacement and, to a lesser extent, anomalous diffraction (AD).[30] The lack of successful mercury-based AD experiments can be partially attributed to the success of other approaches, such as selenomethionine incorporation, but one emerging reason for the failure of mercury in AD experiments is the labile nature of the thiol–mercury bond under X-ray radiation exposure.[31,32]

It was our initial intent to solve the mercury-complex structures with unbiased experimental phases using either isomorphous replacement or AD methods, as this would allow unambiguous identification of mercury sites. Mercury bound crystals were not isomorphous to the native dataset (Table 1) so we adopted a multiwavelength AD strategy. We were unable to obtain interpretable experimental maps and subsequently solved the structure by molecular replacement. Mercury sites in both structures were located by a combination of anomalous difference and omit maps combined with thorough investigation of each putative site's chemical environment. During refinement of both mercury bound structures, it became clear there was significant motion in mercury atoms bound to the introduced cysteine residues. F_o–F_c difference maps (Figure 6(a) and (b)), which show differences between the observed data and model, show small (less than three electrons) "noisy" positive peaks after anisotropic refinement of the individual mercury sites. Based on their small size and proximity to adjacent Hg sites, we attribute these peaks to radiation-induced change of the mercury sites and alternate states of the protein as described above.

The difficulty in using mercury as an anomalous scatterer is due in part to the relative ease with which the mercury–thiol bond is cleaved, so we postulate

that motion in the mercury peaks also reflects radiation damage-induced cleavage of the mercury atoms' interaction with cysteine. A previous radiation damage study on the problems associated with using mercury has seen solvent-exposed mercury atoms "escaping" over time, while those that are buried are more likely to remain bound to their respective sulfur moiety.[32] Using the L170C structure as a test case, we refine the mercury-bound structure against the data derived only from the first 45 frames (72.9% complete; scaled to the entire dataset) and the resulting omit map is shown in Figure 6(c). A comparison with omit maps calculated from all of the data, shows that there is indeed a change in the occupancies of sites. This change in occupancy can be seen as diffusion of mercury out of the solvent accessible channel while the more deeply buried L170C-Hg1 shows little motion.

The consequence of such dynamics is not understood, but it does highlight the need for determining exactly what mercury does upon binding. In the case of T183C, new mutants may be used to probe the role of the interstitial site in the absence of mercury bound in the pore. In L170C we know, at least under X-ray exposure, that mercury is dynamic and influenced by the solvent-filled channel. Here, higher-resolution structures will allow more accurate refinement of occupancies and distances, and functional analysis of new mutants (e.g. double cysteine mutants) can be used to further probe the effect of mercury binding. It will also be important to structurally characterize the role of larger mercurials such as *p*-chloromercuriphenylsulfonic acid, which are extensively used in physiology studies and may have a more complex inhibition mode. Moving away from mercurials, structural studies should be extended to include the recently discovered cationic charged inhibitors, to understand the more general principles of aquaporin inhibition. Such studies may open up new avenues for the discovery of specific small molecule aquaporin inhibitors for clinical use. The mechanisms that we have elucidated and outlined here are a first step towards this important goal.

Materials and Methods

Expression and purification

Mutants of AqpZ were generated by site-directed-mutagenesis of the pET28b-AqpZ construct used in the original structure article.[14] Prior to mutagenesis, endogenous cysteine residues were removed *via* the mutations Cys9Ser and Cys20Ser. The *E. coli* strain C43(DE3) was transformed, grown to 0.6–1 $A_{600\ nm}$ at 37 °C in 2×LB media, 0.5% (v/v) glycerol, 1× M9 salts, and 25 mg/l kanamycin, and induced with 1 mM isopropyl-D-thiogalactoside (Anatrace).[33,34]

All purification was carried out at 4 °C or on ice as necessary. Cells from 6 l of culture were harvested and lysed by a microfluidizer in 20 mM Tris (pH 7.4), 100 mM NaCl, 0.5 mM phenylmethylsulforyl fluoride, 5 mM BME. Membranes were recovered from supernatant by 100,000*g* centrifugation for 2 h. AqpZ was solubilized from membranes by agitation in 20 mM Tris (pH 7.4), 100 mM NaCl, 5 mM BME, 10% glycerol, 270 mM *n*-octyl-β-D-glucopyranoside (OG) (Anatrace) for 12–16 h at 4 °C. Solubilized protein was bound in batch to Ni-NTA resin (Qiagen) for 1 h, washed with 25 resin volumes of 20 mM Tris (pH 7.4), 100 mM NaCl, 5 mM BME, 10% glycerol, 40 mM OG, 20 mM imidazole, and eluted with 20 mM Tris (pH 7.4), 100 mM NaCl, 5 mM BME, 10% glycerol, 40 mM OG, 250 mM imidazole. Imidazole was removed using a Biorad Econo-Pac 10DG desalting column and the 6xHis tag was removed by digestion with 5 μg of trypsin for 12 h at 4 °C. Trypsin was removed by passing over a benzamidine-Sepharose matrix (GE Healthcare), and the protein sample was injected onto a Pharmacia Superose 12 gel filtration column running a mobile phase of 20 mM Tris (pH 7.4), 100 mM NaCl, 2 mM dithiothreitol, 10% glycerol, 40 mM OG. Except as noted, all materials were purchased from Sigma or Fisher. The sample was judged pure and homogeneous by both gel filtration chromatography and Coomassie-stained denaturing gels. Final yields were approximately 10, 7, and 3 mg of protein/l culture for WT, T183C, and L170C, respectively.

Crystalization and data collection

Following gel filtration chromatography, the protein was concentrated to 25 mg/ml using a 30 kDa cutoff Amicon Ultra-15 Centrifugal Filter. Crystals were grown by hanging-drop vapor diffusion at room temperature by 1:1 addition of protein and 25–30% (w/v) polyethylene glycol (PEG) monomethyl ether 2000 (Fluka), 100 mM sodium cacodylate (pH 6.5), and 50–100 mM $MgCl_2$. For co-crystallization, divalent mercury in the form of 1–3 mM $HgCl_2$ was added in batch to the protein sample before mixing with precipitant. In general, the best co-crystals were obtained at slightly lower (2–4%) PEG concentrations than in apo crystallization. Crystals grew to roughly 300 μm×300 μm×150 μm over the course of several days and were flash frozen in liquid nitrogen following a brief washing in the mother liquor plus 15% glycerol for cryoprotection. Diffraction intensities were collected on Advanced Light Source Beamline 8.3.1 using an ADSC Quantum-Q210 CCD detector. Prior to data collection on mercury-complex crystals, fluorescence energy scans of the L_{III} mercury edge were taken to verify mercury substitution.

Phasing and model refinement

Data were processed with Elves[35] and CCP4[36] (using MOSFLM[37]) and the structures were solved by molecular replacement with the published WT structure (Protein Data Bank Code 1RC2) using Phaser.[38] The models were refined with iterative cycles of manual building with Coot[39] and restrained refinement with individual *B*-factor refinement in Refmac5.[40] After several initial rounds of refinement, mercury atoms were located unambiguously by inspecting anomalous difference maps, F_o–F_c omit maps (peaks of 15–7 σ), and the local chemical environment. Following refinement, the appearance of negative density in F_o–F_c difference maps indicated that occupancy for mercury atoms was not unity. Occupancies for mercury atoms, along with their anisotropic *B*-factors were refined using least-squares refinement in SHELXL.[22]

Proteoliposome reconstitution

Before removing the 6xHis tag with trypsin, aliquots of protein were set aside for proteoliposome reconstitution.

E. coli polar lipids were sonicated to clarity and the reconstitution cocktail was prepared by sequentially adding 100 mM Mops (pH 7.5), 51.3 mM OG (1.5%, w/v), 50 μg/ml of purified protein, and 10 mg/ml *E. coli* polar lipids (Avanti).[20] To reduce oxidation, lipid stocks were stored in 2 mM BME and all buffers were under argon atmosphere. Following cocktail incubation for 1 h at room temperature (RT), proteoliposomes were formed by diluting the mixture 50-fold into a running buffer of 20 mM Hepes (pH 7.5) and harvested by centrifugation at 100,000*g* for 2 h. Pelleted liposomes were resuspended into 1 ml of running buffer (20 mM Hepes, pH 7.5) and stored at 4 °C. Liposome monodispersity was verified by dynamic light scattering with a mean diameter of 90 nm.

To analyze the kinetics of water conduction through the channel, we subjected the proteoliposomes to an osmotic gradient by mixing 1:1 proteoliposomes (final AqpZ monomer concentration of 0.27 μM) and running buffer with osmolyte (20 mM Hepes (pH 7.5), 570 mM sucrose) and measured water efflux (liposome shrinkage) by light scattering in a stopped-flow device at 440 nm. Resulting curves were fit to a single-exponential rate constant (k_1) as a measure of conduction to use in comparison between mutants and with inhibitor ($n = 5$, same liposome preparation). Inhibition of the mutants was accomplished by incubating the resuspended proteoliposomes with the appropriate concentration of $HgCl_2$ for 1 h at RT prior to stopped-flow analysis ($n = 5$, same liposome preparation). Data were consistent across multiple protein and liposome preparations.

Protein Data Bank accession codes

The atomic coordinates have been deposited in the RCSB Protein Data Bank and are available under accession codes 209D, 209E, 209F and 209G.

Acknowledgements

We thank Franklin A. Hays, Pascal Egea, Janet Finer-Moore and Zach Newby for helpful manuscript suggestions. D.F.S. was supported by a Burroughs Wellcome Trainee Fellowship. Research was supported by grant GM 24485 from the NIGMS.

References

1. Borgnia, M., Nielsen, S., Engel, A. & Agre, P. (1999). Cellular and molecular biology of the aquaporin water channels. *Annu. Rev. Biochem.* **68**, 425–458.
2. Hille, B. (2001). *Ion Channels of Excitable Membranes*, 3rd edit., Sinauer, Sunderland, Mass.
3. Macey, R. I. (1984). Transport of water and urea in red blood cells. *Am. J. Physiol.* **246**, C195–C203.
4. Zeidel, M. L., Ambudkar, S. V., Smith, B. L. & Agre, P. (1992). Reconstitution of functional water channels in liposomes containing purified red cell CHIP28 protein. *Biochemistry*, **31**, 7436–7440.
5. Preston, G. M., Carroll, T. P., Guggino, W. B. & Agre, P. (1992). Appearance of water channels in *Xenopus* oocytes expressing red cell CHIP28 protein. *Science*, **256**, 385–387.
6. Fushimi, K., Uchida, S., Hara, Y., Hirata, Y., Marumo, F. & Sasaki, S. (1993). Cloning and expression of apical membrane water channel of rat kidney collecting tubule. *Nature*, **361**, 549–552.
7. Javot, H. & Maurel, C. (2002). The role of aquaporins in root water uptake. *Ann. Bot. (Lond.)*, **90**, 301–313.
8. Preston, G. M., Jung, J. S., Guggino, W. B. & Agre, P. (1993). The mercury-sensitive residue at cysteine 189 in the CHIP28 water channel. *J. Biol. Chem.* **268**, 17–20.
9. Kuang, K., Haller, J. F., Shi, G., Kang, F., Cheung, M., Iserovich, P. & Fischbarg, J. (2001). Mercurial sensitivity of aquaporin 1 endofacial loop B residues. *Protein Sci.* **10**, 1627–1634.
10. Fu, D., Libson, A., Miercke, L. J., Weitzman, C., Nollert, P., Krucinski, J. & Stroud, R. M. (2000). Structure of a glycerol-conducting channel and the basis for its selectivity. *Science*, **290**, 481–486.
11. Sui, H., Han, B. G., Lee, J. K., Walian, P. & Jap, B. K. (2001). Structural basis of water-specific transport through the AQP1 water channel. *Nature*, **414**, 872–878.
12. Walz, T., Hirai, T., Murata, K., Heymann, J. B., Mitsuoka, K., Fujiyoshi, Y. *et al.* (1997). The three-dimensional structure of aquaporin-1. *Nature*, **387**, 624–627.
13. Park, J. H. & Saier, M. H., Jr (1996). Phylogenetic characterization of the MIP family of transmembrane channel proteins. *J. Membr. Biol.* **153**, 171–180.
14. Savage, D. F., Egea, P. F., Robles-Colmenares, Y., O'Connell, J. D., 3rd & Stroud, R. M. (2003). Architecture and selectivity in aquaporins: 2.5 Å X-ray structure of aquaporin Z. *PLoS Biol.* **1**, E72.
15. Harries, W. E., Akhavan, D., Miercke, L. J., Khademi, S. & Stroud, R. M. (2004). The channel architecture of aquaporin 0 at a 2.2-Å resolution. *Proc. Natl Acad. Sci. USA*, **101**, 14045–14050.
16. Tornroth-Horsefield, S., Wang, Y., Hedfalk, K., Johanson, U., Karlsson, M., Tajkhorshid, E. *et al.* (2006). Structural mechanism of plant aquaporin gating. *Nature*, **439**, 688–694.
17. Lee, J. K., Kozono, D., Remis, J., Kitagawa, Y., Agre, P. & Stroud, R. M. (2005). Structural basis for conductance by the archaeal aquaporin AqpM at 1.68 Å. *Proc. Natl Acad. Sci. USA*, **102**, 18932–18937.
18. Calamita, G., Bishai, W. R., Preston, G. M., Guggino, W. B. & Agre, P. (1995). Molecular cloning and characterization of AqpZ, a water channel from *Escherichia coli*. *J. Biol. Chem.* **270**, 29063–29066.
19. Borgnia, M. J., Kozono, D., Calamita, G., Maloney, P. C. & Agre, P. (1999). Functional reconstitution and characterization of AqpZ, the *E. coli* water channel protein. *J. Mol. Biol.* **291**, 1169–1179.
20. Borgnia, M. J. & Agre, P. (2001). Reconstitution and functional comparison of purified GlpF and AqpZ, the glycerol and water channels from *Escherichia coli*. *Proc. Natl Acad. Sci. USA*, **98**, 2888–2893.
21. Smart, O. S., Goodfellow, J. M. & Wallace, B. A. (1993). The pore dimensions of gramicidin A. *Biophys. J.* **65**, 2455–2460.
22. Sheldrick, G. M. & Schneider, T. R. (1997). SHELXL: high resolution refinement. *Methods Enzymol.* **277**, 319–343.
23. Emsley, J. (2001). *Nature's Building Blocks: An A-Z Guide to the Elements.* Oxford University Press, Oxford.
24. Zalups, R. K. (2000). Molecular interactions with mercury in the kidney. *Pharmacol. Rev.* **52**, 113–143.
25. Yu, J., Yool, A. J., Schulten, K. & Tajkhorshid, E. (2006). Mechanism of gating and ion conductivity of a possible tetrameric pore in aquaporin-1. *Structure*, **14**, 1411–1423.

26. Cooper, G. J. & Boron, W. F. (1998). Effect of PCMBS on CO2 permeability of *Xenopus* oocytes expressing aquaporin 1 or its C189S mutant. *Am. J. Physiol.* **275**, C1481–C1486.
27. Doyle, D. A., Morais Cabral, J., Pfuetzner, R. A., Kuo, A., Gulbis, J. M., Cohen, S. L. *et al.* (1998). The structure of the potassium channel: molecular basis of K+ conduction and selectivity. *Science*, **280**, 69–77.
28. Niemietz, C. M. & Tyerman, S. D. (2002). New potent inhibitors of aquaporins: silver and gold compounds inhibit aquaporins of plant and human origin. *FEBS Letters*, **531**, 443–447.
29. Yool, A. J., Brokl, O. H., Pannabecker, T. L., Dantzler, W. H. & Stamer, W. D. (2002). Tetraethylammonium block of water flux in Aquaporin-1 channels expressed in kidney thin limbs of Henle's loop and a kidney-derived cell line. *BMC Physiol.* **2**, 4.
30. Blundell, T. L. & Johnson, L. N. (1976). *Protein Crystallography,* Academic Press, New York.
31. Ji, X., Blaszczyk, J. & Chen, X. (2001). The absorption edge of protein-bound mercury and a double-edge strategy for HgMAD data acquisition. *Acta Crystallog. sect. D*, **57**, 1003–1007.
32. Ramagopal, U. A., Dauter, Z., Thirumuruhan, R., Fedorov, E. & Almo, S. C. (2005). Radiation-induced site-specific damage of mercury derivatives: phasing and implications. *Acta Crystallog. sect. D*, **61**, 1289–1298.
33. Miroux, B. & Walker, J. E. (1996). Over-production of proteins in *Escherichia coli*: mutant hosts that allow synthesis of some membrane proteins and globular proteins at high levels. *J. Mol. Biol.* **260**, 289–298.
34. Mohanty, A. K. & Wiener, M. C. (2004). Membrane protein expression and production: effects of polyhistidine tag length and position. *Protein Expr. Purif.* **33**, 311–325.
35. Holton, J. & Alber, T. (2004). Automated protein crystal structure determination using ELVES. *Proc. Natl Acad. Sci. USA*, **101**, 1537–1542.
36. (1994). The CCP4 suite: programs for protein crystallography. *Acta Crystallog. sect. D*, **50**, 760–763.
37. Leslie, A. G. (2006). The integration of macromolecular diffraction data. *Acta Crystallog. sect. D*, **62**, 48–57.
38. Read, R. J. (2001). Pushing the boundaries of molecular replacement with maximum likelihood. *Acta Crystallog. sect. D*, **57**, 1373–1382.
39. Emsley, P. & Cowtan, K. (2004). Coot: model-building tools for molecular graphics. *Acta Crystallog. sect. D*, **60**, 2126–2132.
40. Murshudov, G. N., Vagin, A. A. & Dodson, E. J. (1997). Refinement of macromolecular structures by the maximum-likelihood method. *Acta Crystallog. sect. D*, **53**, 240–255.

Edited by J. Bowie

(Received 14 December 2006; received in revised form 19 February 2007; accepted 20 February 2007)
Available online 2 March 2007